Influence of Rotating Wheels and Moving Ground Use on the Unsteady Wake of a Small-Scale Road Vehicle

Aleksandra Anna Rejniak[1] · **Alvin Gatto**[1]

Abstract

New insights into how different ground simulation methods affect road vehicle aerodynamics are presented. Experiments are conducted on a 1/24th-scale model, representative of a Heavy Goods Vehicle, at a Reynolds number, based on width of 2.3×10^5. Particular focus lay in characterising differences in unsteady wake development, with mean drag, base pressures, and wake velocities quantified, compared, and evaluated. Distinctly, these tests include the effects of elevated blockage ratio and wheel rotation. Results show moving ground use can have a substantial influence under these conditions, with increases in wake length and average base pressure coefficient of 17% and 9%, respectively. The dominant wake dynamics, characterised by a global streamwise oscillation commonly referenced as the bubble pumping mode, was also found dependent with asymmetric shedding frequencies from both vertical and horizontal base edges higher with static ground use. For these conditions, development of a low-frequency turbulence source, near omni-directional in nature, positioned behind the model, further contaminates the flow-field. This feature disappears with moving ground use. Both the nature and characteristics of the turbulence generated behind the wheels were also found to evolve differently, with a moving ground promoting stronger and more defined oscillatory behaviour up to model mid-height, two-and-a-half widths downstream. Overall, these results highlight that while variations in time-independent quantities to differing ground simulation can often be very subtle, prompting the interpretation of negligible overall effects, in-depth consideration from a time-dependent perspective may lead to a different conclusion.

Keywords Moving ground · Ground simulation · Rotating wheels · Road vehicle · Unsteady wake

1 Introduction

Reducing the aerodynamic drag of road vehicles is a crucial activity underpinning current efforts to mitigate the future impact of climate change. Within the UK alone, these vehicles emit more than 110 million tonnes of CO_2 annually, almost one-third of the

---

✉ Aleksandra Anna Rejniak
  aleksandra.rejniak@brunel.ac.uk

[1] Department of Mechanical and Aerospace Engineering, Brunel University London, Uxbridge, UK

carbon budget for the country (National Statistics 2019). Heavy goods vehicles (HGVs) make a significant contribution accounting for approximately 17% (HM Government 2011), despite representing less than 1.6% of traffic volume (Department for Transport 2017). Developing low drag technologies for these vehicles will be vital to achieving sustainable future economic and ecological prosperity.

A high-fidelity test environment is essential to low drag concept development. This is best served by testing at full-scale (Grover and Visser 2006; Leuschen and Cooper 2006), however, intrusive expense, insufficient data fidelity, physical size and weight complications make this difficult to routinely realise in practice (Britcher et al. 2014). Instead, designers tend to rely on Computational Fluid Dynamics (CFD) and wind tunnel testing to guide development (Horrigan et al. 2007, 2008; McCallen et al. 2000). The first of these, CFD, remains an invaluable tool, particularly when interrogating complex flows, however, the grid sizes required, especially for detailed time-dependent analysis (Salati et al. 2015; Krajnović and Davidson 2004), are normally very large, difficult to setup, and time consuming to run (Bayraktar and Bayraktar 2006; Cooper 2004); all not ideal for a rapidly changing design space. This leaves the designer use of the wind tunnel.

Wind tunnels have informed road vehicle aerodynamic design for many decades. They can range in size from the very small (< 1 m^2 test section area), where capital investment and operating costs are low, to the very large (> 100 m^2 test section area), where this is less so. Common to most is the forced movement of air over a stationary model; a situation somewhat atypical to reality where the vehicle is moving, and as such, the generation of additional boundary layers (in particular on the wind tunnel floor) can be problematic (Cogotti 1999; Mercker and Wiedemann 1990). This is particularly the case if they are allowed to interact with the model, adversely impacting attempts to replicate true aerodynamic performance (Le Good et al. 1998; Leuschen 2013).

Use of a moving ground (MG) can largely eliminate this issue. These facilities work by imposing surface motion (normally with a moving belt) to hinder floor boundary layer formation (Burgin et al. 1986; Wiedemann and Potthoff 2003). Employed mostly within the motorsport and automotive industries however, they are rarely adopted within HGV aerodynamic design. This is due in part to technical difficulties (i.e. mounting, need for wheel rotation, etc.), particularly at larger scales, but also the general perception that accurate ground simulation is not needed given their larger ride height; an assumption yet to be comprehensively validated (Britcher et al. 2014; Leuschen 2013; Wood 2015). Instead, use of a stationary ground (SG) is more common. This setup is nominally simpler to construct, provides minimal mounting interference (typically from underneath) and negates the need for wheel rotation (Hucho and Sovran 1993).

However, differences exist between these two test conditions for many configurations, including HGV test models, leading to questions of the validity of stationary ground use. Le Good et al. (1998), Fago et al. (1991), Sardou (1987), Forbes et al. (2017) and Krajnović and Davidson (2005) have all noted reduced drag with moving ground use, whereas Geropp and Odenthal (2000) reported a dependency on Reynolds number, and Zhang et al. (2014) an increase; the latter reflecting the prevention of viscous underbody blockage (from boundary layer formation) increasing local velocities. Leuschen (2013) provided similar reasoning for a drag increase with a moving ground in operation finding also notable cab roof deflector and side extender drag sensitivity. Burgin et al. (1986), Strachan et al. (2007), and Söderblom et al. (2009) have likewise demonstrated increases, with Fago et al. (1991) also providing evidence for drag insensitivity beyond $G/H > 0.1$, where G is ground clearance and H, model height.

Previous work also shows the surrounding flow-field can be affected. Lajos et al. (1986) reported additional downward momentum (along model sides and aft) with moving ground use due to increased momentum flux generated within the underbody region. These effects were absent using a stationary ground; instead, strongly retarded flow in the underbody-floor gap was characteristic, promoting side outflow. Movement of the rear wall stagnation point from the upper half (SG) to the bottom half (MG) on the rear wall was also observed representing a significant modification to the wake flow. Similar work by Duell and George (1993) identified a 2–8% lower base pressure coefficient in this area between moving and stationary ground use; the result dependent on ground clearance, with Krajnović and Davidson (2005) showing a flow periodicity dependency.

The influence of wheel rotation is another aspect generally omitted (Hucho and Sovran 1993; Willemsen et al. 2011). This is despite strong evidence from existing work citing its importance (together with a moving ground) for accurate reproduction of realistic flow conditions (Burgin et al. 1986; Söderblom et al. 2009, 2012; Wickern et al. 1997; Waeschle 2007). Devesa and Indinger (2012), Le Good et al. (1998), and Willemsen et al. (2011) all found drag reductions with wheel rotation with Wiedemann (1996) highlighting body-shape, and Willemsen et al. (2011) ride height, as defining influences. Söderblom et al. (2009, 2012) also observed reduced inner wheel housing static pressures with rotating wheels, as well as modifications to the local flow both upstream and downstream; the consequence of which modifies subsequent downstream structures. Faster velocities and a smaller wake behind rotating wheels has also been noted by Anbarci et al. (2013), with Devesa and Indinger (2012) indicating only limited influences localised around the wheels and in the size of flow separation regions.

From the perspective of unsteady wake behaviour, wheel rotation and moving ground use invite other questions. Square-back geometries typically form highly oscillatory and characteristically unsteady wake phenomenon (bi-stability, pumping, asymmetric shedding, shear layer instabilities, etc.) as highlighted by the work of Volpe et al. (2015), Khalighi et al. (2001), Perry et al. (2016), Wang et al. (2020), Pavia et al. (2017), Pavia and Passmore (2018), Grandemange et al. (2013) and Duell and George (1993, 1999). However, many details of how, if at all, these processes are affected by such additions continue to remain unresolved. This is particularly evident for tests performed at high model solid blockage ratios characteristic to many previous HGV investigations (Britcher et al. 2014; Leuschen 2013; Martini et al. 2014; Stephens and Babinsky 2016; Storms et al. 2001).

This work seeks to provide insight into how different ground simulation techniques and wheel rotation affect the unsteady wake of a HGV-representative sub-scale model. Experiments are conducted at a high solid model blockage ratio with relative differences between drag coefficients, base pressures, and wake dynamics captured, explored, and quantified. Particular focus lay in quantifying, from a time-dependent perspective, distinct disparities in the nature of developed turbulent structures and their impact on the wider flow-field. Localised wheel wake dynamics are also considered within this framework along with how dissimilar ground simulation techniques impact streamwise evolution.

2 Experimental Setup and Apparatus

2.1 The Model

The simplified 1/24th-scale model used for all experiments is shown in Fig. 1. This baseline model, representative of a commercial HGV, neglects fine detail and incorporates a streamlined front tractor profile based on the Global Transportation System (GTS) (Storms et al. 2001) to reduce the possibility of strong leading edge separation. The model is constructed from Perspex and Aluminium in two parts: a tractor and trailer bottom section, and a trailer. These two sections were designed to make contact at three points to allow the trailer to 'free-float' via a load cell and connecting rod at the front face, and two sliding links positioned rearward (either side of model centreline). Eight fully rotating aluminium wheels (four rearmost uncovered), supported by four steel axles, contact the ground. The width (W) of the model is 110 mm. Height (H) and Length (L) are 1.42 W and 4.55 W respectively.

An aerodynamically streamlined support strut affixed atop the trailer located the model inside the test section. This support extended through the wind tunnel roof being mounted externally (Fig. 2). The thickness-to-chord ratio is 0.25 (chord = 0.36 W, length = 1.85 W) and is positioned at the model centreline, $x^* = 2.18$ (* indicating dimensions normalised by model width) downstream of the tractor front face. The same aerofoil profile adopted by Strachan et al. (2007) is used. The model is positioned at the wind tunnel centreline $(y^* = 0)$, with the front face $x^* = 3.3$ downstream of a flow splitter front edge (Fig. 2).

2.2 Wind Tunnel

All tests were conducted in a closed test section (1.3 m long, 0.46 m wide, and 0.36 m high), open-circuit wind tunnel. The freestream velocity chosen was $U_\infty = 30$ m/s, giving a Reynolds number based on body width of $Re_W = 2.3 \times 10^5$ ($Re_H = 3 \times 10^5$, $Re_L = 1.02 \times 10^6$). Freestream uniformity, turbulence intensity, and heightwise velocity consistency at a
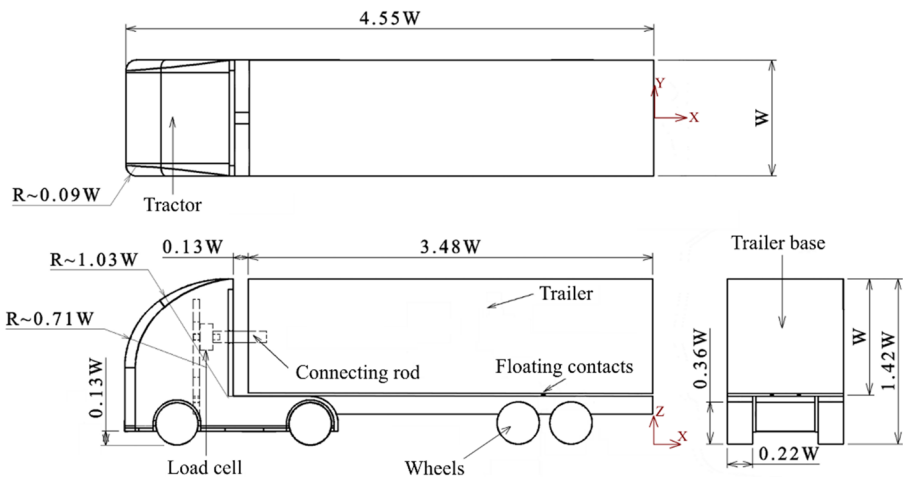

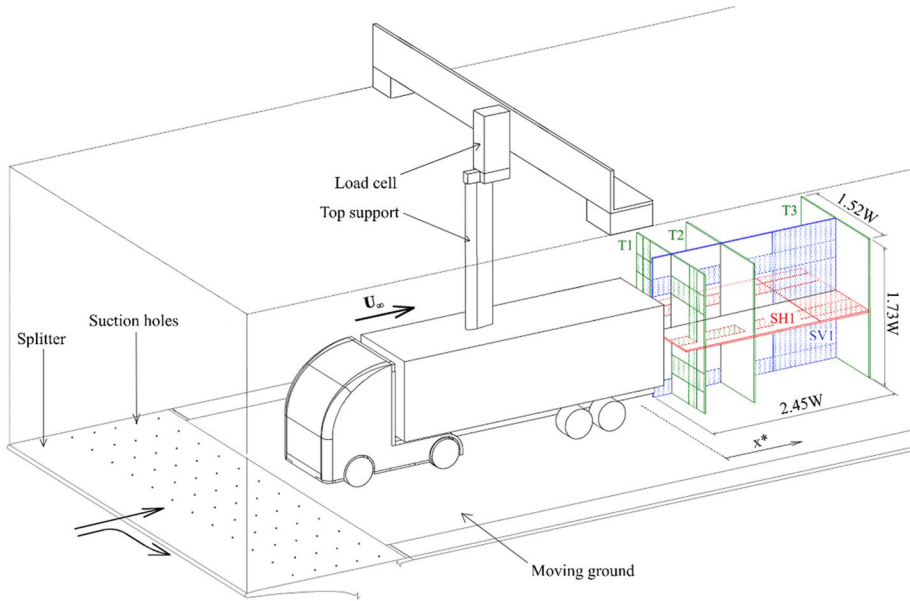**Fig. 1** Schematic of the baseline model

Fig. 2 Schematic of the model setup and hot-wire measurement planes

central test section (empty) position are $\pm 1\%$, 0.5%, and $\pm 1\%$, respectively. Solid blockage ratio, based on projected frontal area, is 11.1%, remaining below the 15% upper limit as suggested by SAE J1252 (2012). Given the direct comparative nature of this study, no corrections to the data have been applied. However, a quantitative assessment of this influence was made using Mercker's method (Mercker 1986; Söderblom et al. 2016). These findings indicated a maximum correction (reduction) to presented drag and pressure coefficients of 20%, and Strouhal number (St_w) of 9.5%. Additionally, prior to the main testing programme, assessment of both total model and trailer drag coefficient (denoted by C_{DM} and C_{DT} respectively) sensitivity to Reynolds number was also determined. These results are presented in Fig. 3. As shown, for $Re_W > 1.2 \times 10^5$, both show only a weak dependence irrespective of ground condition.

Fig. 3 Variation of drag coefficient with Reynolds number; C_{DM} (solid), C_{DT} (dashed)
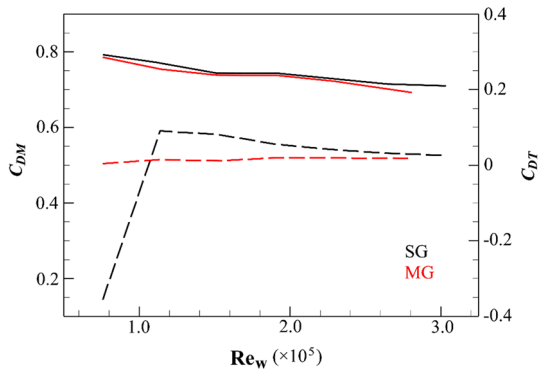
A moving ground is fitted. This facility produces a freestream velocity profile within $0.9 < u^* < 1$ a distance $z^* \geq 0.045$ above ground level. Corresponding boundary layer displacement thickness when idle (SG—test section empty) is $z^* = 0.02$ at the model base location. The moving ground is $x^* = 7.5$ long, $y^* = 3.27$ wide, and centrally mounted (Fig. 2). Belt speed is matched to freestream velocity within ± 1 m/s with motion precipitating wheel rotation. LabVIEW software monitored operation.

To further reduce upstream boundary layer development, a front splitter is located upstream of the moving ground (Fig. 2). Suction holes embedded within its top surface aid boundary layer suppression with air drawn though a perforated plate located underneath the belt used to prevent inadvertent lifting during operation. Cooling water is circulated through this plate to aid heat rejection.

2.3 Load Cells

Two load cells were used to measure total model and isolated trailer drag. Total model drag is obtained by a Tedea Huntleigh load cell (full scale output of 196 N) affixed directly to the top support strut and supported externally by the wind tunnel roof (Fig. 2). This fixture was adjustable to allow careful placement of the model so that the wheels made only light contact with the belt surface. This position was chosen to reduce stationary ground surface friction to an absolute minimum and ensure the smallest possible effect on drag. This methodology was selected over a non-contact configuration due to the high probability for flow ingress between wheels and ground. A Model 31 single axis tension/compression load cell (full scale output of 44 N) was mounted between tractor and trailer (see Fig. 1) to measure isolated trailer drag (the result determined by subtraction from total drag). Calibration of each cell was performed in situ with a maximum load up to 10 N used to assess accuracy. Initially, eleven equally-spaced calibration steps up to 1.2 N were applied to calibrate trailer drag. A further 10 equally-spaced steps up to 10 N were applied thereafter for total drag. These ranges were selected to coincide with expectations. All points were sampled at 20 kHz and averaged over 40 s with this process repeated three times to assess variability. Uncertainty estimates, encompassing overall repeatability, thermal drift, and non-linearity, to 95% confidence were $\Delta C_{DM} = \pm 0.018$ (± 10 N range) and $\Delta C_{DT} = \pm 0.010$ (± 1.2 N range) respectively, with drag coefficients determined from:

$$C_{DM} = \frac{2D_M}{\rho U_\infty^2 A}, C_{DT} = \frac{2D_T}{\rho U_\infty^2 A} \tag{1}$$

where D_M, D_T, ρ, U_∞, and A, are total model and trailer drag force, ambient air density, freestream velocity, and model cross-sectional area respectively.

All drag measurements made during wind tunnel testing were sampled at 20 kHz for 20 s providing 400,000 samples for data analysis. Both initial and final 'wind-off' load measurements were used for data correction as recommended in SAE J1252 (2012). Additional tests performed using a dummy support strut extending down to, but not touching the top of the trailer (2 mm separation), and with the model fixed by a rear-mounted support sting, were used to correct for support tare.

2.4 Hot-Wire Anemometry

Hot-wire anemometry (HWA) was chosen as the main flow analysis tool. All tests employed a dual-sensor X-wire probe positioned using an automated 3D traverse system (resolution 0.01 mm). Probe calibration prior to each wind tunnel test was performed against a computer-controlled Dantec$^©$ precision pneumatic flow unit (resolution 0.1 m/s). A velocity calibration range encompassing 0.5–40 m/s was used throughout with polynomial coefficients determined by 20-point curve-fitting. To ensure utmost measurement precision and accuracy, a separate directional calibration was performed to determine yaw factors with the probe axis varied between $-40°$ and $40°$ ($5°$ increments). Maximum velocity uncertainty to 95% confidence was ± 1 m/s ($\Delta u^* = \pm 0.033$, * denotes normalised by freestream velocity, U_∞). All results are presented corrected for ambient temperature variations with an overheat ratio set to 0.8 (Jørgensen 2002).

The decision to use HWA primarily was based on the ability of the technique to provide high frequency spectral content, at reasonable cost, to small spatial resolution. No attempts are made to resolve accurately flow direction within reversed velocity flow regions (recirculating wake, etc.), however, general inference in terms of velocity magnitude and spectral content is offered in line with previous studies (Duell and George 1993, 1999; Khalighi et al. 2001; Castelain et al. 2018). Outside these areas, all data presented lie well within the maximum limits ($u_{rms}^* < 0.3$, $u_{rms}/u < 0.5$) specified by Chandrsuda and Bradshaw (1981).

Measurements were taken at five different planes: three transverse planes (T1-3), one streamwise vertical plane (SV1), and one streamwise horizontal plane (SH1). The size and position of these planes are described in Fig. 2 and Table 1. Measurement points were selected equally-spaced throughout (0.091 W), however, a finer resolution (0.045 W) was chosen in areas of specific interest (i.e. separated shear layers, etc.) to allow more detailed interrogation (hatched areas in Fig. 2). Grid spacing was also increased (0.18 W) in other areas to reduce test duration where possible. These point distributions are summarised in Table 2. To minimise the likelihood of probe damage, a lower limit of $z^* = 0.091$ was set for all planes with sensor wires located $x^* = 0.73$ upstream of the probe vertical support strut. All hot-wire data was sampled at 20 kHz for 20 s with load data acquired over the same time interval. All hot-wire results are presented interpolated by a factor of two (using Gaussian process regression) to enhance feature detail.

2.5 Pressure Measurements

Surface pressures were measured on the trailer base at 64 equally spaced locations (Fig. 4) using a Scanivalve MPS-4264. Each surface tap is 0.8 mm in diameter and connected to the Scanivalve by 90 mm long silicon tubing (1 mm ID). Prior to testing,

Table 1 Specifications for hot-wire measurement planes

	T1	T2	T3	SV1	SH1
x*	0.41	1.11	2.59	0.14–2.59	0.14–2.59
y*	− 0.76–0.76	− 0.76–0.76	− 0.76–0.76	0	−0.76–0.76
z*	0.09–1.82	0.09–1.82	0.09–1.82	0.09–1.82	0.92
No. positions	528	360	360	552	552

Table 2 Grid spacing detail for hot-wire measurement planes (0.091 W everywhere else)

Alternate grid spacing	0.045 W	0.18 W
T1	0.41 < y* < 0.59 − 0.59 < y* < − 0.41 0.45 < z* < 0.64 1.45 < z* < 1.64	–
SV1	0.09 < z* < 0.27 1.36 < z* < 1.55	1.55 < x* < 2.45
SH1	− 0.59 < y* < − 0.36 0.36 < y* < 0.59	1.73 < x* < 2.45

Fig. 4 Base pressure measurements positions
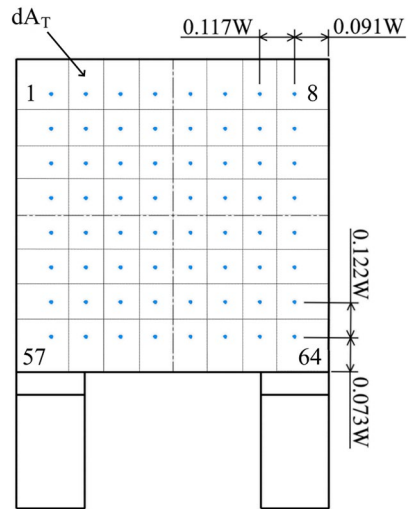
the frequency response characteristics of the connecting tube were assessed against a Bruel and Kjaer 4133 laboratory standard microphone up to 400 Hz. All results presented were corrected for these variations using a similar methodology to that adopted by Sims-Williams and Dominy (1998).

A custom-built wireless communication system designed to fit inside the trailer is used to transmit sampled data to a laptop PC. This system used a battery-powered Belkin N100 wireless access point to relay 60 s of data sampled at 800 Hz. This provided 48,000 measurement points for subsequent post-processing. Reference static pressure was taken at a port located on the side of the wind tunnel directly adjacent to the trailer base. A single piece of connecting pneumatic tube, which extended out the trailer and test section, is used for this purpose. All results are presented averaged over three separate wind tunnel test runs with pressure measurements made independent of hot-wire and drag measurements. Maximum pressure coefficient measurement uncertainty is $\Delta Cp = \pm 0.006$ to a 95% confidence level, with Cp and Cp_{rms} defined by:

$$C_P = \frac{2(p' - p_\infty)}{\rho U_\infty^2}, C_{Prms} = \sqrt{\frac{\sum_1^n \left(C_P - \overline{C_P}\right)^2}{n}} \qquad (2)$$

where p', p_∞, and n are the instantaneous and freestream static pressures respectively for n samples ($^-$ denotes the ensemble average).

3 Results and Discussion

3.1 Drag Coefficients

Table 3 summarises mean drag coefficient results obtained for both moving and stationary ground configurations. The influence of the moving ground use is shown to reduce, marginally, both measurements; although C_{DM} variation is noted to be within experimental uncertainty. Fago et al. (1991), Le Good et al. (1998), Sardou (1987), Krajnović and Davidson (2005), and Geropp and Odenthal (2000) all found a similar trend. The trailer itself is shown to make a small contribution to total drag for each condition, with a maximum 5.6% for the stationary ground case. This is more than double that observed for moving ground use (2.6%) with both being lower than expected at full-scale [≈ 25%—(Patten et al. 2012)]. One of many factors can account for this result. Martini et al. (2014), McCallen et al. (2000), Frank and Turney (2016), and Pankajakshan et al. (2016) all highlight a strong dependence of tractor-trailer gap on trailer drag. For the current setup, this was chosen atypically small (0.13 W) to minimise any likelihood of significant flow unsteadiness, not related to the wake flow, developing and degrading load cell signal quality. With such a small gap however, lower pressures are known to develop in this region producing two similar, but opposing effects: increased tractor drag due to exposure to its back surface, and reduced trailer drag from exposure to its front face (Martini et al. 2014; Pankajakshan et al. 2016). Frank and Turney (2016) also show this effect can be significant, with a trailer absent any undercarriage/wheel contributions (similar to the current setup) being an overall negative contributor to total drag. Reynolds number and elevated solid model blockage ratio can also be further contributory factors (Wood 2015; Zdravkovich 2003).

3.2 Time-Averaged Base Pressure Coefficients

Mean and rms static pressure coefficient variations over the trailer base are presented in Fig. 5. Vehicle centreline ($y^* = 0$) relative difference comparisons are also included (Fig. 5c). For both test cases, Cp contours show many topological similarities. Both indicate a large area of low pressure acting within $0.5 < z^* < 1.1$, as well as an isolated region of higher pressure located at a top centreline location ($1.3 < z^* < 1.35$). This topology is well known and agrees with that reported previously (Horrigan et al. 2007; Storms et al. 2001; Bayraktar et al. 2005;

Table 3 Total model and trailer drag coefficients for stationary and moving ground conditions

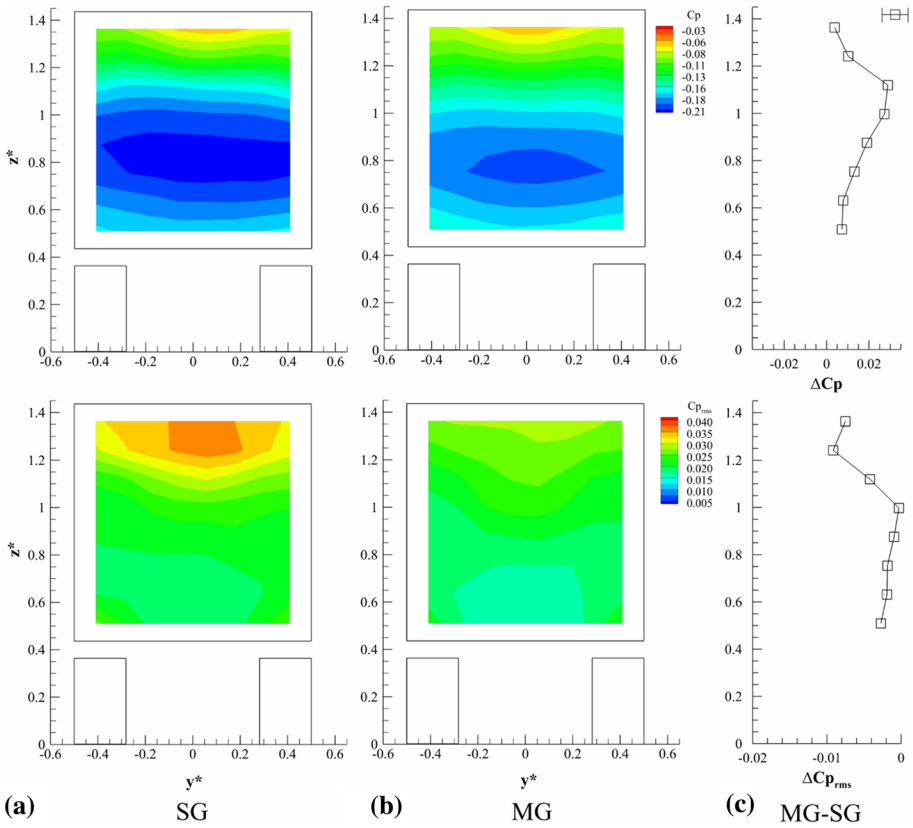|	C_{DM} (± 0.018)	C_{DT} (± 0.010)
SG	0.729	0.041
MG	0.723	0.019

Fig. 5 Trailer base pressure coefficient results: **a** SG; **b** MG; **c** MG-SG difference along y*=0

McCallen et al. 1999; Gutierrez et al. 1996) as the result of the recirculating wake structure encompassing a proximate bottom vortex core responsible for the minimum Cp magnitudes identified at z* ≈ 0.7–0.8, and upper recirculating flow impingement, for higher magnitudes adjacent to the top edge [y* ≈ 0, z* ≈ 1.35—(Perry et al. 2016; Pavia et al. 2017; Castelain et al. 2018)]. The former appears subtly more pronounced for the stationary ground case, suggesting a stronger influence. The implications of this finding will be discussed further in Sect. 3.3. Figure 5c further quantifies differences at y*=0 between these two conditions. A maximum variation of ΔCp ≈ 0.03 is shown just above the base centre (z* ≈ 1.1) signifying an increase with moving ground use. Reduced C_{DT} (Table 3) supports this finding, as does the increase (9%) in average base pressure coefficient ($-C_{Pb}$) and the same, but corresponding decrease, in trailer base pressure drag coefficient (C_{DTbase}); the latter obtained from:

$$C_{DTbase} = -\frac{1}{A}\int Cp \cdot dA_T \approx -\frac{1}{A}\sum_{i=1}^{N} Cp \cdot dA_T \qquad (3)$$

Table 4 Average base pressure and trailer base pressure drag coefficients for stationary and moving ground conditions

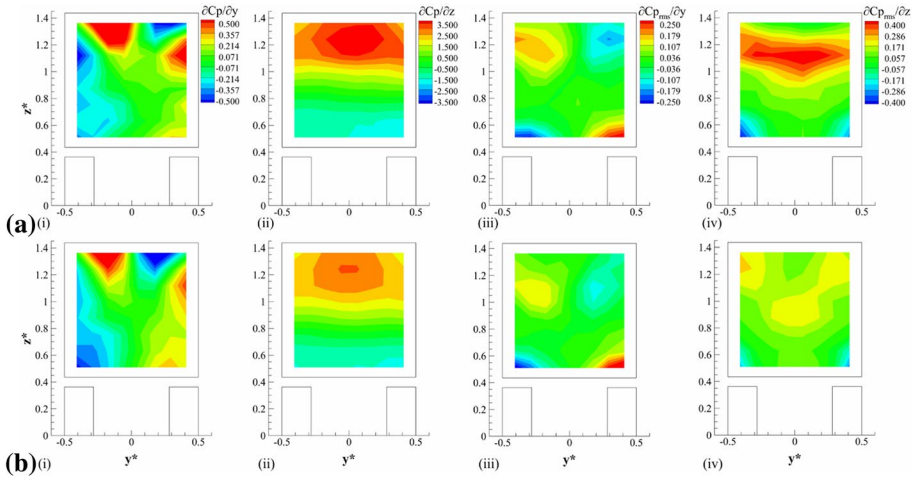|	$-C_{Pb}\ (\pm 0.006)$	C_{DTbase}
SG	0.169	0.118
MG	0.154	0.107

Fig. 6 Spatial base pressure coefficient gradients: **a** SG; **b** MG; (i) $\partial Cp/\partial y$, (ii) $\partial Cp/\partial z$, (iii) $\partial Cp_{rms}/\partial y$, (iv) $\partial Cp_{rms}/\partial z$

Comparing C_{DTbase} (Table 4) and C_{DM} (Table 3) shows that the influence of the tractor-trailer gap at reducing overall trailer drag is indeed significant as discussed in Sect. 3.1, with C_{DTbase} alone responsible for up to 16% (SG) of total drag.

Contours of Cp_{rms} also show a similar, subtle, variance. A comparative increase for the stationary case near the top ($1 < z^* < 1.35$), consistent with more intense unsteady recirculating flow impingement on the base (Lajos et al. 1986; Perry et al. 2016; Wang et al. 2020; Pavia and Passmore 2018; McArthur et al. 2016), is evident in Fig. 5c. This implies moving ground use has another effect under these conditions—impart flow stability to this area (maximum $\Delta Cp_{rms} \approx -0.01$ at $z^* \approx 1.25$). The influence appears very localised, with results outside this region ($z^* < 1$) showing limited variation.

Further elucidation into more subtle features and stimuli can be garnered through crosswise and heightwise spatial gradient distributions presented in Fig. 6. At first glance, topologies again appear generally similar, however, with close inspection, several distinct characteristics are revealed. Firstly, regions subtending the top edges ($|y^*| \approx 0.1$–0.3, $z^* \approx 1.35$) and sides [$|y^*| \approx 0.3$–0.4, $0.8 < z^* < 1.1$—Fig. 6a, b(i)] exhibit little change indicating insensitivity to moving ground use. Within locations directly above the wheels ($|y^*| \approx 0.3$–0.4, $0.5 < z^* < 0.6$) however, some sensitivity does exist (albeit weak). This is particularly evident for $\partial Cp/\partial y$, which indicates marginally more wheel wake influence at these locations. The mechanism responsible for this result is discussed in Sect. 3.3.

Heightwise Cp gradient distributions shown in Fig. 6a, b(ii) appear markedly less chaotic with a transition from negative to positive magnitudes with increasing height. These results reflect the significant heightwise pressure variations imparted by the wake to the

base (i.e. low-pressure vortex core proximity at the bottom shifting to higher pressure flow impingement at the top) (Wang et al. 2020; Pavia and Passmore 2018). The significance of these changes is also reflected in $\partial Cp/\partial z$ magnitudes being an order higher than $\partial Cp/\partial y$. Upper base regions ($z^* > 1$) also appear more affected for stationary ground test conditions [Fig. 6a(ii)] suggesting stronger impingement than with moving ground use. This result, taken together with those presented in Fig. 5 for Cp, tend to support development of a more compact wake with use of a stationary ground.

Crosswise Cp_{rms} spatial gradients are also provided [Fig. 6a, b(iii)]. Unsteady wheel wake signatures are captured for both test cases (|y*| ≈ 0.35, z* ≈ 0.55) with no indications of crosswise sensitivity to ground condition. Upper side-edge locations (|y*| ≈ 0.1–0.4, 1.1 < z* < 1.3) indicate more elevated $\partial Cp_{rms}/\partial y$ for the stationary ground case [Fig. 6a(iii)] with no compatible trend found in Fig. 6b(iii). These differences reflect a stronger rise in developed unsteadiness as evidenced by Fig. 5a. Correspondingly, moving ground use [Fig. 6b(iii)] within the same region indicates much weaker, more distributed $\partial Cp_{rms}/\partial y$ magnitudes, largely displaced to lower base positions (|y*| ≈ 0.1–0.4, 1 < z* < 1.2). This confirms a shift towards more quiescent base flow exposure under these conditions. Pavia and Passmore (2018) identified a similar stabilising effect on the wake of a Windsor body with rotating wheels.

Heightwise Cp_{rms} gradients also show evidence of the unsteady wheel wake behaviour at bottom base corners (|y*| ≈ 0.35, z* ≈ 0.55). Comparing Fig. 6a(iv) to b(iv), this influence appears more pronounced for the stationary ground case suggesting a weak heightwise sensitivity to moving ground use. Further implications of this finding are discussed in Sect. 3.4.4. High gradients are also found at upper base locations (1 < z* < 1.3) indicating distinctly more pronounced flow unsteadiness imparted to the base within the region. Based on these results and those presented for Cp and $C_{DM,DT}$, the conclusion of general insensitivity to dissimilar ground simulation appears obvious. As will be shown in following sections, this assertion can be deceptively simplistic, particularly when considering results from a time-dependent perspective.

3.3 Time-Averaged Wake Characteristics

Connections to the time-averaged wake are now explored with streamwise velocity magnitudes (T1-T3) presented in Fig. 7. Overall, these results confirm general expectations with lowest u* mapping downstream wake development. The influence of the supporting strut is also captured (T1 - y* ≈ 0, z* > 1.5). Mean flow symmetry about y*=0 appears preserved, with an invariant wake height and bounding freestream flow, either side, and over the top of the model, characteristic. At T1, broad regions of low velocity magnitude flow (u* < 0.35) closely align with the trailer base. These regions represent measurements made within the recirculating flow region with lowest u* magnitudes found to reside within the bottom half (y*=0, z* < 0.8). This coincides with the position of Cp minima identified in Fig. 5. Further downstream at T2, the wake is seen to extend to ground level, eventually closing by T3.

Comparing ground conditions (Fig. 7a, b), several distinct disparities exist. First, and as would be expected, the presence of the boundary layer for the stationary ground case is significant. This is represented by the increasingly prominent area of lower velocity magnitude fluid below z* ≈ 0.25 either side of the model (|y*| > 0.5). At T3 [Fig. 7a(iii)], this feature is most obvious. With moving ground use, remnants persist but exhibit far less impact
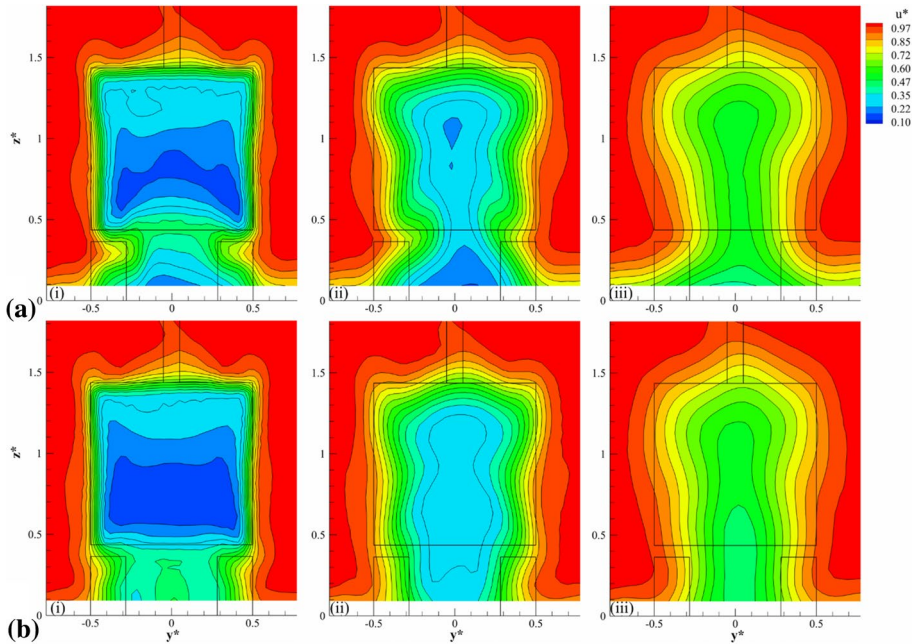
Fig. 7 Results for u* with: **a** SG, **b** MG; at T1 (i), T2 (ii), and T3 (iii)

on the surrounding flow. This is reflected most notably by a more consistent wake width near ground level [Fig. 7b(iii)].

A second distinguishing feature is a region of low velocity magnitude fluid that develops directly beneath the trailer without the moving ground in operation. This is particularly evident for planes T1 and T2 encompassing |y*| < 0.3 and z* < 0.3. Sardou (1986) identified a similar phenomenon behind a car model using a stationary ground as a 'Ground Delamination Bubble'. The phrase 'Ground Separation Region (GSR)' is adopted in this work. McArthur et al. (2016) also describe a similar phenomenon with reducing ground clearance, as does Castelain et al. (2018) with lower underbody mass flux. In each case, a strong ground adverse pressure gradient precipitates development. Significant upwash emanating towards the lower-pressure base wake is also characteristic. This can be identified in Fig. 7a(i) by the 'arch-like' distortion at |y*| < 0.4 and 0.5 < z* < 0.6. The GSR is shown to dominate the lower wake at T1 [|y*| < 0.4 at z* ≈ 0.5—Fig. 7a(i)], merge with the base wake at T2 [Fig. 7a(ii)], having only limited impact at T3 [y* ≈ 0, z* ≈ 0.1—Fig. 7a(iii)]. No evidence of the GSR, at any plane, exists with the moving ground in use [Fig. 7b(i–iii)].

Another more subtle distinction resides within the wheel/trailer junction area for T1 (|y*| ≈ 0.3–0.5 at 0.2 < z* < 0.4) with stationary ground use [Fig. 7a(i)]. The flow more rapidly entrains towards the vehicle centreline in this area triggering a localised wake width contraction at z* ≈ 0.3. This feature originates from flow around, and in-between, the rear wheels and bottom trailer surface either side of the model, leading to encroachment of higher velocity flow below each bottom base corner [|y*| ≈ 0.4 at z* ≈ 0.3—Fig. 7a(i)]. This action would explain the reduced wheel wake influence discussed previously with stationary ground use [Fig. 6a(i)]. The same behaviour is not shown with moving ground use; instead a near constant wake width, with more uniform underbody flow predominates [Fig. 7b(i)]. This contraction persists downstream to T2 [Fig. 7a(ii)], and subsequently T3

[Fig. 7a(iii)], where the general wake form exhibits notably more inconsistent width with height.

Figures 8 and 9 present differences within T1-T3 at selected locations. Positive magnitude differences indicate faster (or higher u_{rms}*) flow characteristics relative to the stationary ground case, and negative—slower (or lower u_{rms}*). Figure 8a shows most variability below $z^* \approx 0.8$ at T1. The flow is notably faster for the stationary ground case ($\Delta u^* \approx -0.2$) at $z^* \approx 0.5$ as the upwash emanating from underneath the trailer entrains towards the base wake. This is seen to quickly reverse towards lower z^* positions reaching maximum at $z^* = 0.091$ where development of the GSR and boundary layer are suppressed with moving ground use. This trend persists further downstream with diminishing variability ($\Delta u^* \approx \pm 0.1$ at T3).

The results of u_{rms}* and Δu_{rms}* (MG-SG) show additional features [Fig. 8b(i-iii)]. Elevated u_{rms}* magnitudes at $z^* \approx 1.42$ identify the top shear layer which undergoes progressive broadening with downstream development. This feature indicates little sensitivity to moving ground use suggesting no significant disparity in boundary layer thickness between the two configurations, at the base position prior to separation, exists. There is, however, evidence of significant variability below ($z^* < 0.8$ at T2), with reductions in streamwise flow unsteadiness [Δu_{rms}* = -0.07—Fig. 8b(ii)]. These results add further evidence to the trend already discussed in Sect. 3.2. At either preceding [T1—Fig. 8b(i)] or following planes [T3—Fig. 8b(iii)], only limited sensitivity to ground condition exists.
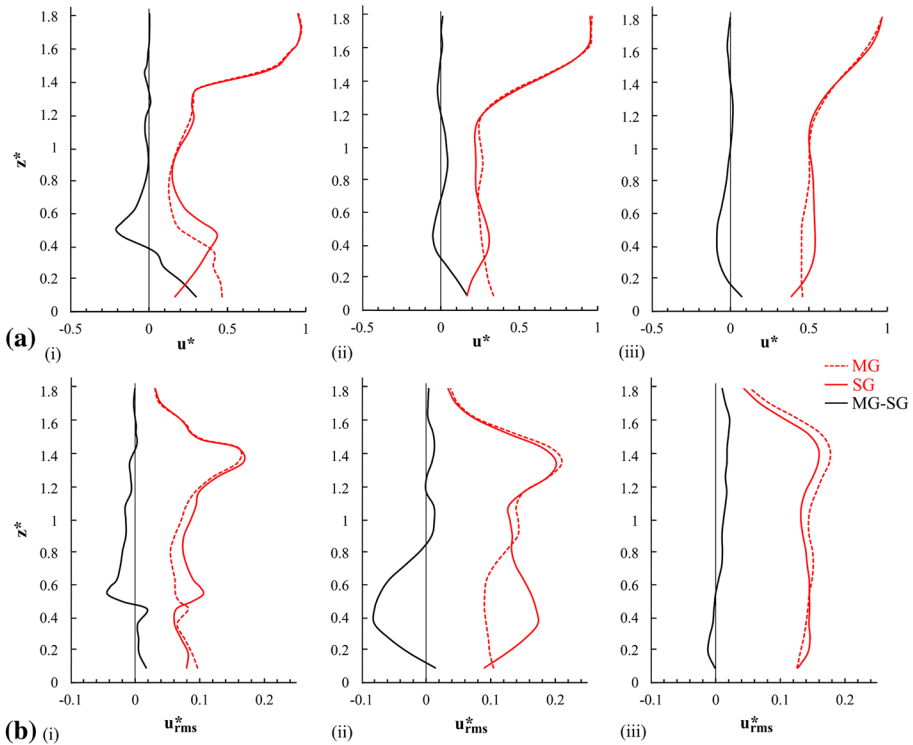

Fig. 8 Comparisons at y*=0 between **a** Δu* (MG-SG) and **b** Δu$_{rms}$*, for transverse planes T1 (i), T2 (ii), and T3 (iii)
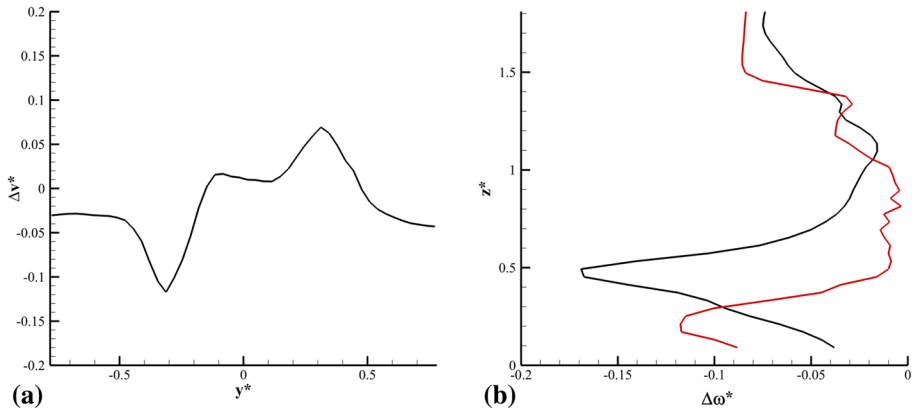
Fig. 9 Difference between MG and SG conditions at T1: **a** Δv^* at $z^* = 0.3$, **b** $\Delta \omega^*$ at $y^* = 0$ (black) and $y^* = -0.4$ (red)

Figure 9 highlights differences in v^* and ω^* magnitudes within the wheel/trailer interface area identified in Fig. 7a. Results are presented at $z^* = 0.3$ (Fig. 9a), $y^* = -0.4$ and $y^* = 0$ (Fig. 9b) respectively. Maximum Δv^* between the two ground conditions is significant, with an additional $\Delta v^* \approx 0.07$–0.11 directed towards the vehicle centreline for the stationary ground case; a small bias favouring the left side. This effect is precipitated by the additional upwash generated, with Fig. 9b quantifying these changes ($\Delta \omega^*$) at both $y^* = 0$ and $y^* = -0.4$. Differences are comparable to that identified in Δu^* by Fig. 8a(i), with $\Delta \omega^* \approx -0.17$ at vehicle centreline ($y^* = 0$). A significant crosswise impact is also preserved with $\Delta \omega^* \approx -0.12$ found behind the rear wheels close to the ground ($y^* = -0.4$, $z^* \approx 0.2$).

Contours of Mean Turbulent Kinetic Energy normalised by U_∞^2 (K) presented in Fig. 10 provide further insight. These results show a similar inwardly-skewed wake topology behind the wheels, but also highlight important differences in the nature of K production with different ground conditions. Both Fig. 10a and b show elevated K directly behind the wheels, however, the former indicates significantly lower peak magnitudes. This is caused by the disruptive interaction resulting from the enhanced crossflow under these conditions. As shown in Fig. 10b for the moving ground case, these characteristics are absent; instead more elevated, and concentrated K, is characteristic ($|y^*| \approx 0.4$, $z^* \approx 0.2$). Higher K is also observed at upper side edge locations ($|y^*| \approx 0.4$–0.5, $0.7 < z^* < 1.4$) in Fig. 10a. This identifies differences in shear layers flow unsteadiness for this test case providing further support for results discussed in Sect. 3.2.

Topologies of streamwise wake evolution at SV1 add further detail (Fig. 11). Results from this perspective again show the wake represented by lower velocity magnitudes ($u^* < 0.35$) emanating from the trailer rear and convecting downstream. Lowest u^* for both flow cases again exist adjacent to the base at $z^* \approx 0.8$ in agreement with previous findings. Undisturbed freestream flow pervades above model height ($z^* > 1.6$) with the GSR centred at $x^* \approx 0.75$, subtending the region $0.1 < x^* < 2.3$ and $z^* < 0.5$. The merging of the GSR and base wake already identified in plane T2 [Fig. 7a(ii)] is shown, as is the region of intense upwash generated by flow emanating from underneath the trailer ($x^* \approx 0.3$, $z^* \approx 0.5$).
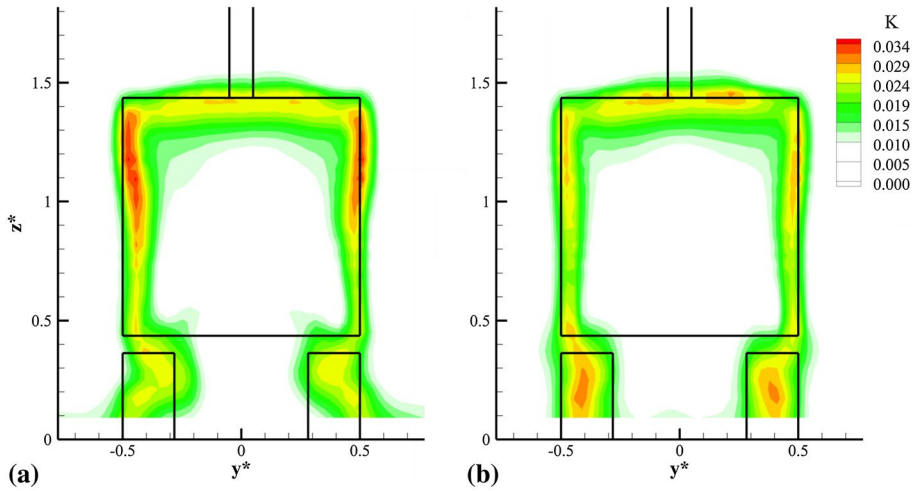
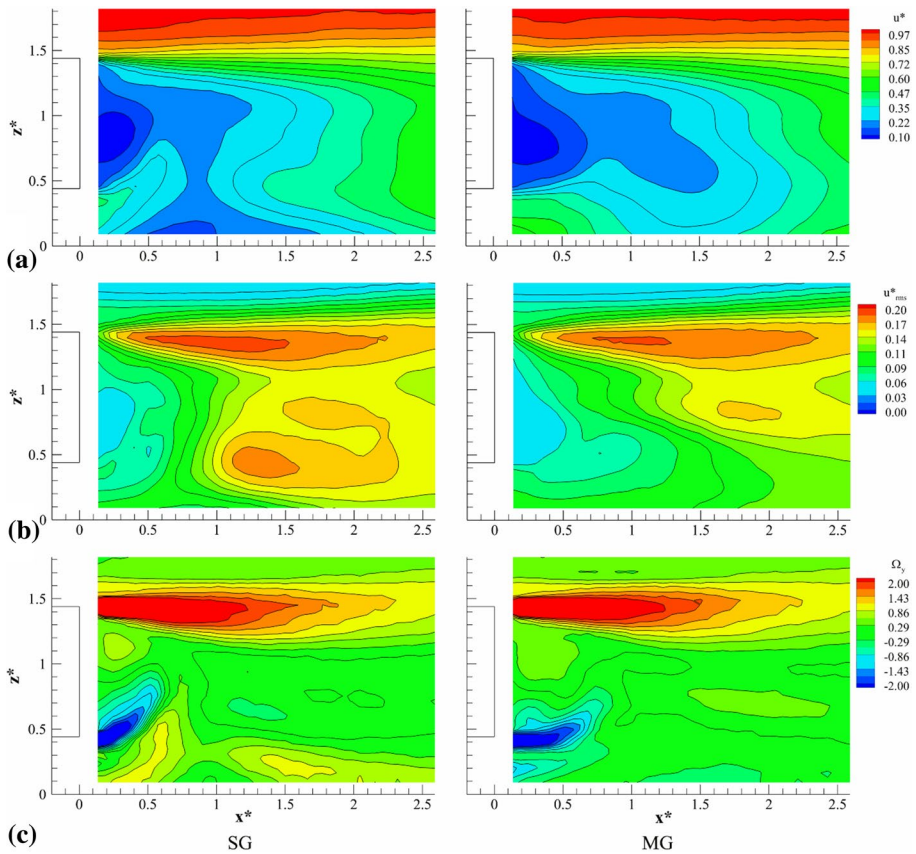**Fig. 10** Normalised Mean Turbulent Kinetic Energy (K) at plane T1 for: **a** SG and **b** MG test conditions

Fig. 11 Contours at SV1 for SG and MG conditions: **a** u^*, **b** u_{rms}^*, and **c** Ω_y

Figure 11b provides comparative u_{rms}^* contours for the same plane. Elevated u_{rms}^* downstream of the top edge ($1.2 < z^* < 1.5$, $0.2 < x^* < 2.5$) again identifies the top shear layer. Similar topologies to those observed in Fig. 8b confirm limited sensitivity to moving ground use. Below, and nearer ground level, the presence of the GSR ($0.5 < x^* < 1.5$, $0.2 < z^* < 1$) is captured and found to precede increased levels of u_{rms}^* which persist downstream ($1 < x^* < 2.55$, $z^* < 0.7$). Maximum Δu_{rms} (≈ 0.18) is shown at $x^* \approx 1.25$, $z^* \approx 0.45$ immediately downstream of the lower trailer base wake and GSR locations. The same characteristics are not shown in Fig. 8b suggesting that these interactions play an important role in precipitating the increase.

Further details are provided by crosswise vorticity results (Ω_y—normalised by W/U_∞) presented in Fig. 11c. As would be expected, strongest Ω_y coincides within the upper separated shear layer and from underneath the trailer; both regions representing the tendency of the wake flow to achieve closure. Fundamental differences in the upwash characteristics are clearest from this perspective with orientations of Ω_y significantly different between the two ground conditions; moving ground use being decidedly more horizontal (Fig. 11c). This would be the expectation of the combined influence of more effective underbody flow and removal of the GSR, resulting in a shift in the wake balance. Regions of weaker co-rotating vorticity directly upstream and downstream of the GSR ($x^* \approx 0.5$, $z^* \approx 0.2$ and $x^* \approx 1.6$, $z^* \approx 0.2$—Fig. 11c—SG) are also notable, precipitated most probably, as a consequence of the preceding upwash, and subsequent downwash.

A further perspective is provided by results for the SH1 plane shown in Fig. 12. Moving ground use exhibits a much more subtle influence from this perspective with all results showing similar topologies. The separated wake is identifiable once again from the topology of lowest velocity magnitudes. Excellent crosswise flow symmetry is evident with separating shear layers from both side edges captured (Fig. 12b). Heightwise vorticity contours (Ω_z) are also very similar (Fig. 12c), with weak counter-rotating vorticity signatures ($x^* \approx 0.65$–0.75, $|y^*| \approx 0.2$) evident. Qualitatively, these suggest that wake length increases with moving ground use.

Figure 13 considers this assertion more quantitatively with the presentation of streamwise variations of both u^* and u_{rms}^* ($y^* = 0$—SH1). Duell and George (1993, 1999) show such variations can be used to determine the position of the free stagnation point as the point of combined u^* minima and u_{rms}^* maxima; recirculation length, x_r^*, being the distance from that point to the model base. From these results, a 17% increase from $x_r^* \approx 1.19$ to $x_r^* \approx 1.39$ is evident with moving ground use.

3.4 Time-Resolved Flow Characteristics

The influence of ground condition on the unsteady wake characteristics is now considered. Base pressure spectra are considered initially, then the general wake dynamics, and finally detailed wake velocity spectra within selected areas of interest. All pressure spectra were obtained from the average of 15 time segments (1.25 s duration) using a Hamming window and 50% overlap. Velocity spectra were averaged from 39 time segments (0.5 s duration) using an identical procedure. Bin widths are $\Delta St_W = 0.0014$ and $\Delta St_W = 0.0022$ respectively. Selected results are presented with offset magnitudes to aid interpretation with Strouhal number defined as:
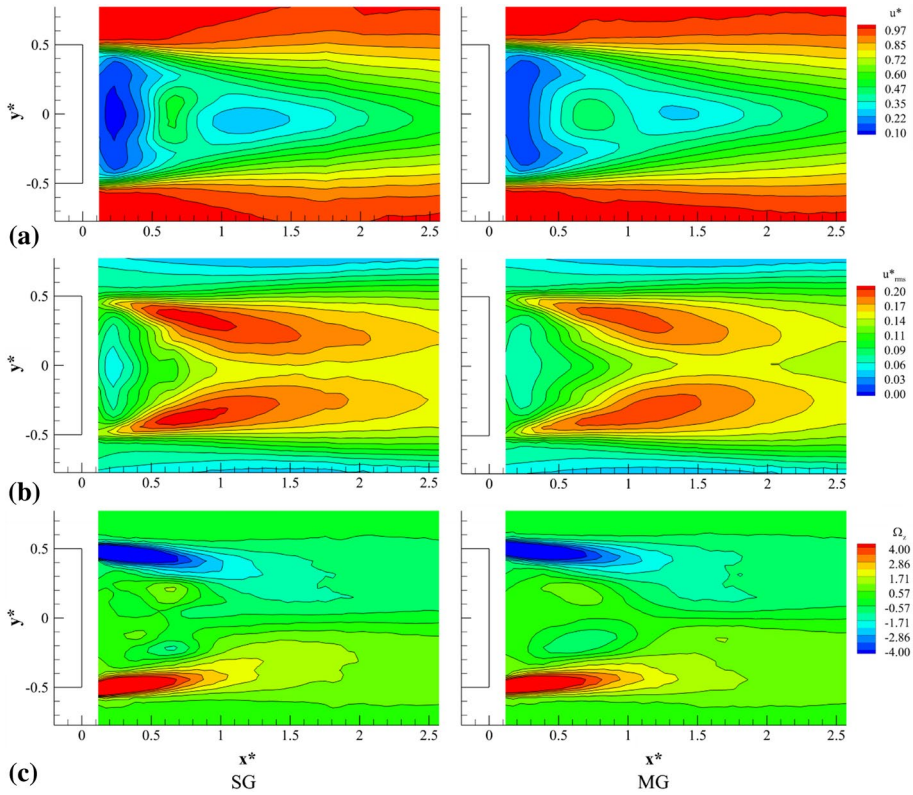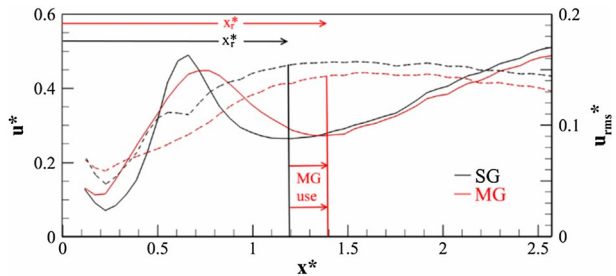
$$St_w = \frac{fW}{U_\infty}$$

(4)

Fig. 12 Contours at SH1 for SG and MG conditions: **a** u*, **b** u_{rms}*, and **c** Ω_z

Fig. 13 Determination of x_r*; u* (solid), u_{rms}* (dashed) at y*=0 – SH1

where f is the frequency of flow oscillation.

3.4.1 Base Pressure Spectra

Figure 14 presents selected pressure spectra around base periphery and centre. Wind-off condition spectra are also included at position 1 for comparison (belt on for MG case). Generally, results indicate little spanwise and heightwise variation with a notable exception being higher spectral magnitudes ($St_w > 0.3$) above rear wheel locations (57, 64). These

results reflect the localised wheel wake unsteadiness present for both ground conditions captured in Fig. 6 and discussed in Sect. 3.2. Clearly defined oscillatory behaviour appears absent at all locations, particularly below $St_w < 0.3$, where expected wake shedding and bubble pumping mechanisms can be typical (Volpe et al. 2015; Khalighi et al. 2001; Duell and George 1999; McArthur et al. 2016). Close inspection does however reveal, subtle, broad peaks located at $St_w \approx 0.107$ and $St_w \approx 0.123$ ($St_H \approx 0.138$ and $St_H \approx 0.178$) for stationary and moving ground conditions respectively. These signatures are discernible at most locations [particularly base mid-height and centre (25–40)], inferring a near global influence. Duell and George (1993, 1999) describe similar characteristics for the wake bubble pumping mechanism at $St_w = 0.069$, as do Volpe et al. (2015) ($St_w \approx 0.11$), Khalighi et al. (2001) ($St_w \approx 0.098$), McArthur et al. (2016) ($St_w \approx 0.08$) and Pavia et al. (2017) ($St_w \approx 0.094$), at similar Strouhal numbers on various other models. Of particular interest to this study is the 17% increase in St_w with moving ground use; identical to that observed for Δx_r^* (Fig. 13).

3.4.2 General Wake Dynamics

Further elucidation into the nature of these spectra is provided by base pressure coherence and phase (Fig. 15b), as well as through presentation of wake velocity spectra (Fig. 15c, d) at selected positions [Fig. 15a(i–iv)]. Coherence and phase relationships were obtained from:

$$\gamma_{1-2}^2 = \frac{|S_{1-2}|^2}{|S_{1-1}S_{2-2}|}, \phi_{1-2} = \arctan\left(\frac{\text{Im}[S_{1-2}]}{\text{Re}[S_{1-2}]}\right) \qquad (5)$$

where S_{1-1} and S_{2-2} are the auto-spectra of signals 1 and 2 respectively, and S_{1-2}, the cross-spectrum.

Figure 15b identifies strong coherence ($\gamma^2 \approx 0.5$) between mid-base trailer vertical edge locations (25–32) at the frequencies identified in Sect. 3.4.1. Spectra at these positions are shown to act in-phase, typical of the wake pumping mode (Duell and George 1993, 1999; Khalighi et al. 2001). No other significant flow oscillations are immediately
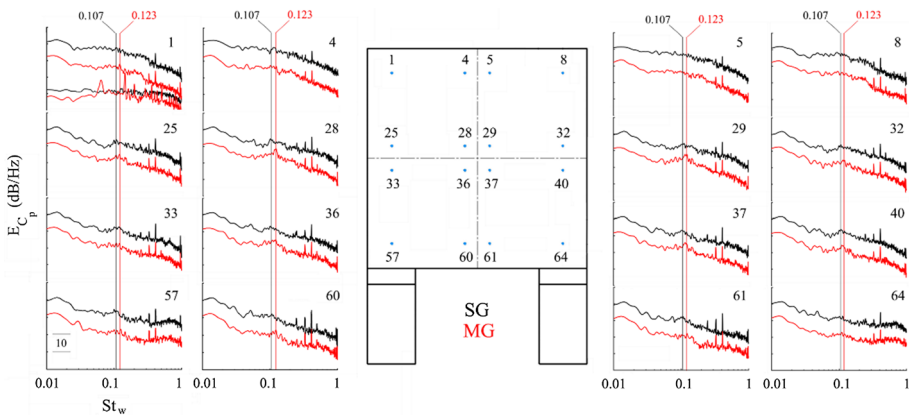

Fig. 14 Base pressure spectra (MG results offset by − 10 dB/Hz to aid interpretation)
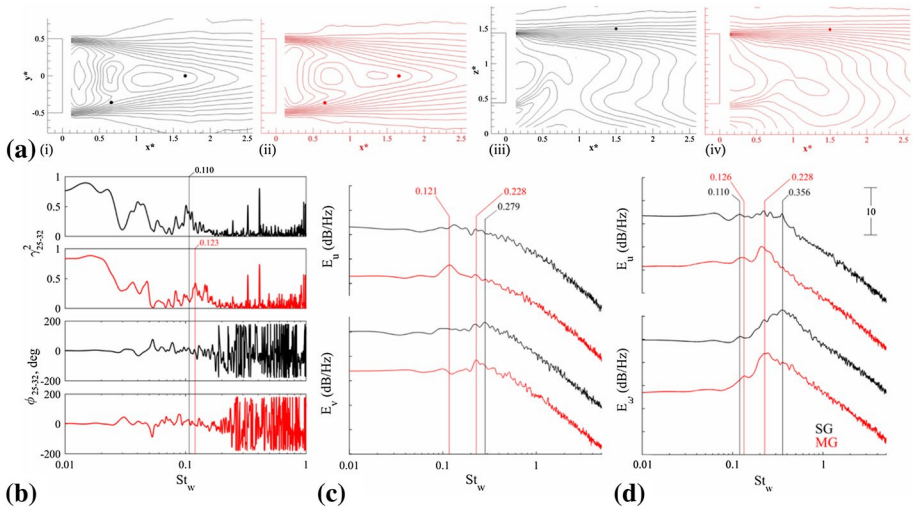
Fig. 15 General wake dynamics: **a** wake velocity spectra locations; **b** base pressure coherence and phase relationships between positions 25 and 32; **c** E_u at $x^* = 0.65$, $y^* = -0.35$ and E_v at $x^* = 1.65$, $y^* = 0$; **d** E_u and E_ω at $x^* = 1.5$, $z^* = 1.5$ (MG spectra offset by -10 dB/Hz to aid interpretation)

obvious from these results for either ground condition, suggesting either their absence or weakness at these positions.

Various wake velocity spectra are presented in Fig. 15c, d. These results confirm that both, weakly defined lateral wake shedding is present ($St_w \approx 0.228$ (MG), $St_w \approx 0.279$ (SG)—Fig. 15c) at Strouhal numbers in general agreement to those of Volpe et al. (2015) ($St_w \approx 0.18$), McArthur et al. (2016) ($St_w \approx 0.17$) and Grandemange et al. (2013) ($St_w \approx 0.17$), along with the bubble pumping mode, identified in Fig. 14, with moving ground use ($St_w \approx 0.121$—Fig. 15c). The complimentary peak at $St_w \approx 0.107$ (Fig. 14) for the stationary ground case is not clear. These findings confer three interesting insights; (1) the bubble pumping mode with stationary ground use is weaker; (2) at $St_w \approx 0.28$, the shedding is less coherent for the stationary ground case, and; (3) the crosswise shedding process is sensitive to ground condition, being 18% lower ($St_w \approx 0.23$) with moving ground use. These results highlight not only that these test conditions, including the development of the GSR, can have a significant influence on the wake dynamics, but confirm the strong inter-dependency of these motions with good agreement to other variations already observed (bubble pumping St_w, x_r^*).

Nominated streamwise and heightwise velocity spectra (E_u, E_ω) at $y^* = 0$ within the top shear layer [see Fig. 15a(iii–iv)] are also shown in Fig. 15d. Many of the same wake dynamics are present. The dissimilar frequencies representative of wake pumping are apparent ($St_w \approx 0.110$ (SG), $St_w \approx 0.126$ (MG)), as is the frequency from vertical base edges at $St_w \approx 0.228$—MG (E_ω—Fig. 15d). This latter peak is shown more narrowband and intense. Conversely, for stationary ground test conditions, E_u and E_ω appear much more broadband in nature, typical of more incoherent processes (Zdravkovich 1997). This is particularly the case for E_u which is largely devoid of defined oscillatory behaviour. A substantial increase in heightwise shedding to $St_w \approx 0.356$ (E_ω) with stationary ground use is also notable, indicating some sensitivity to frequency magnitude from ground condition.

Further insight into the nature of the wake dynamics is provided using Proper Orthogonal Decomposition (POD) (Lumley et al. 1967). This statistical analysis technique allows segregation of the dominant oscillatory modes as well as formulation of a contributory energy budget. Unsteady base pressure data is used.

Figure 16 provides the first four modes. These results confirm the first mode as an in-phase, global wake oscillation, typical of the bubble pumping oscillation (Duell and George 1993, 1999). This mechanism is the most dominant, accounting for between 32.6% (SG) to 40.6% (MG) of base pressure energy content; moving ground use itself accounting for approximately one-third more. Subsequent modes are weaker, with Modes 2 and 3 representative of heightwise and crosswise wake shedding (flapping) processes respectively, and Mode 4, a symmetrically-centred oscillation. Mode 2 accounts for marginally more energy (SG—9.85%, MG—8.94%) than Mode 3 (SG—6.42%, MG—6.89%), confirming this as the stronger asymmetric shedding process.

Topologies within the last two modes show most difference between stationary and moving ground use. Crosswise shedding dynamics (Mode 3) appears materially affected with a chaotic, heightwise asymmetric topology [Fig. 16a(iii)] being replaced by more organised, opposing cells, localised within the top half of the base with moving ground use [Fig. 16b(iii)]. These results support the transition from less to more organised lateral shedding with moving ground in operation already identified in Fig. 15c, and that, for the latter in particular, this process is model-height dependent.

3.4.3 GSR Influence

To better understand the nature of the influence of the GSR and wheel wake dynamics between moving and stationary ground use, further detail is provided through detailed spectral analysis. This section considers the GSR.

Selected streamwise and heightwise velocity spectra from plane SV1 are presented in Fig. 17. Results include positions upstream, within, downstream, and above, denoted by (a)–(k). Directly adjacent to the underbody flow region (a), E_u is observed to be
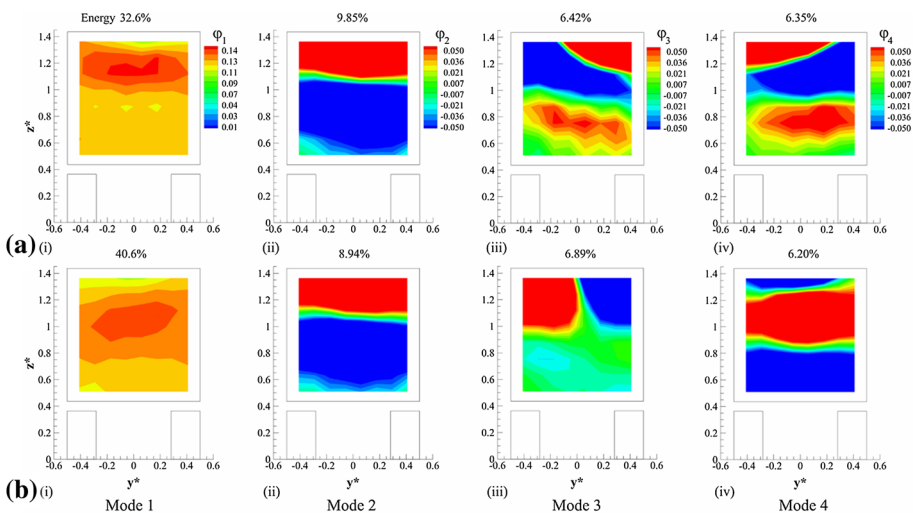

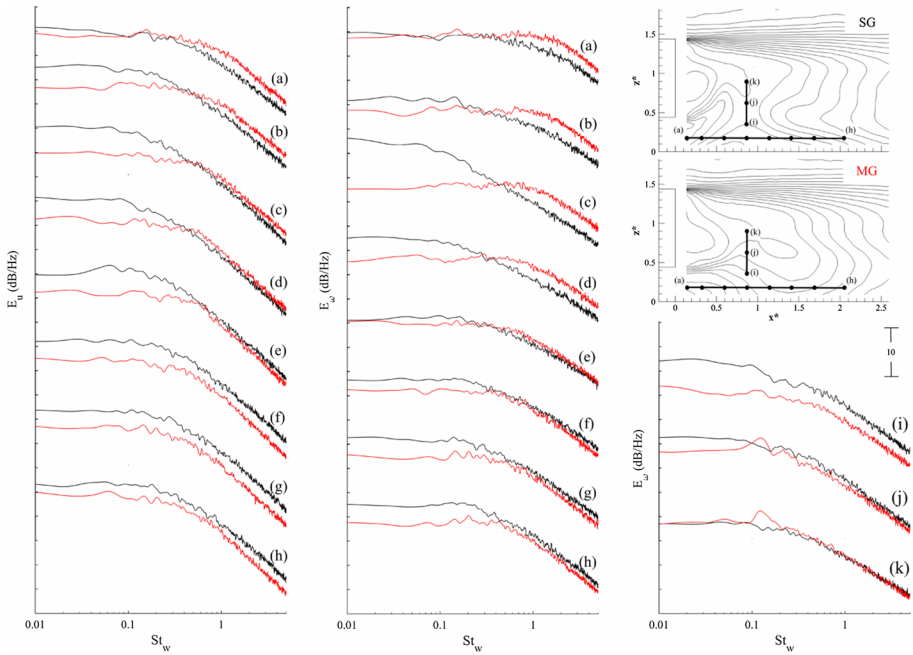**Fig. 16** POD of the first 4 modes: **a** SG; **b** MG

Fig. 17 Selected E_u and E_ω along $0.15 < x^* < 2.08$ at $z^* = 0.18$ and $0.36 < z^* < 0.91$ at $x^* = 0.86$

similar between both ground conditions with marginally higher magnitudes beyond $St_w > 0.3$ for the moving ground case. This would be typical to more effective under-body flow inducing additional, higher frequency turbulence components, underneath the model. These characteristics are shown to persist downstream to (b), with a strong increase in E_u (≈ 5 dB) below $St_w \approx 0.5$ for the stationary ground case; these attributes remaining consistent to location (e). These qualities suggest the GSR is a source of lower-frequency, larger-scale, turbulent structures. These characteristics change upon exit at (f) with spectra further downstream (g–h) showing near constant offset magnitude reductions (2–5 dB) reflective of suppressed boundary layer development with moving ground use.

E_ω shows similar characteristics at the same locations (a–h). These results localise the GSR influence more narrowly to $0.6 < x^* < 0.8$ (b–d) with differences in spectra at $x^* \approx 0.6$ (c) more than 10 dB higher for stationary ground conditions ($St_w < 0.5$); these features synonymous with E_u. These findings further suggest a GSR influence almost omni-directional in nature increasing flow unsteadiness to the region. This would explain the results obtained from Cp_{rms}, $\partial Cp_{rms}/\partial z$, $u_{rms}*$, and K observed in Figs. 5, 6, 8 and 10. Further downstream at (e) spectra appear identical, with position (f), and subsequently (g–h), showing moving ground use acts largely to suppress low frequency flow energies (≈ 5 dB for $St_w < 0.5$), most likely by GSR removal. Height-wise movement from position (i) to (j) shows again similar characteristics to those at lower positions, with no clear distinctions between different ground conditions at (k) aside from the prominence of the bubble pumping mode with moving ground use ($St_w \approx 0.126$).

3.4.4 Influence of Rotating Wheels

Velocity spectra within a region behind the wheels are considered next. Only results for the left wheels are presented for brevity. Figure 18 provides data for positions extending laterally across the wheel profile (a–e), as well as directly above (f–h). Location (a) shows significantly lower E_u at all frequencies with moving ground conditions reflecting reduced boundary layer influence and subsequent flow interactions with the model. Further lateral movement indicates these differences dissipate with insensitivity to ground condition evident at (c). With stationary ground use, elevated E_u below $St_w \approx 1$ is most characteristic at the next position (d) typical to the influence of GSR proximity discussed previously (Sect. 3.4.3). These characteristics persists to (e) with subsequent, higher positions (f–g), exhibiting a general insensitivity to moving ground use.

Similar spatial variations exist for E_v. Higher magnitude offsets at positions (a) and (b) again reflect the significance of boundary layer interactions with stationary ground use. Elevated E_v is most obvious for $St_w > 0.3$ for moving ground conditions showing larger magnitudes with a maximum at $St_w \approx 1.2$ for position (c). This frequency coincides with expected lateral wheel wake shedding ($St_w \approx 1.1$) based on wheel width. Two stronger, more discrete peaks, at $St_w \approx 0.92$ and $St_w \approx 1.28$ are also shown. The first corresponds to the wheel rotation frequency ($St_w \approx 0.87$) with the second remaining somewhat uncertain (possibly a resonant half harmonic). The former remains discernible at position (f), as well as (g), directly above the wheel. Positions entering the underbody flow region (d–e) also capture the lateral wheel shedding with moving ground use, although much weaker, more broadband, and at a reduced central frequency ($0.75 < St_w < 0.9$).

Heightwise variations of E_v show a more abrupt transformation (c, f–h) to broader spectra with moving ground use. For these conditions, position (c) shows the strongest and most
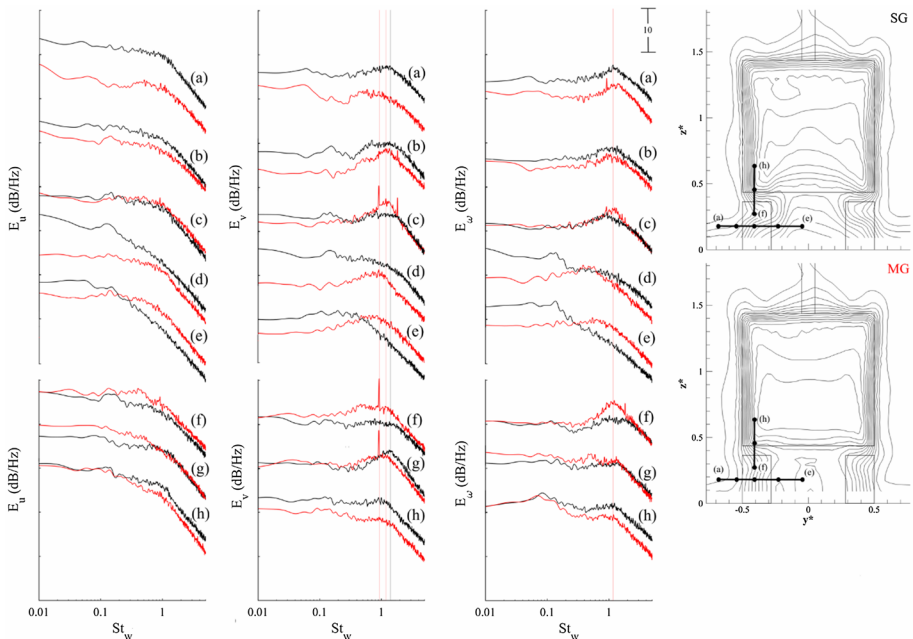

Fig. 18 Selected E_u, E_v, and E_ω along $-0.68 < y^* < -0.045$ at $z^* = 0.18$ and $0.27 < z^* < 0.63$ at $y^* = -0.41$
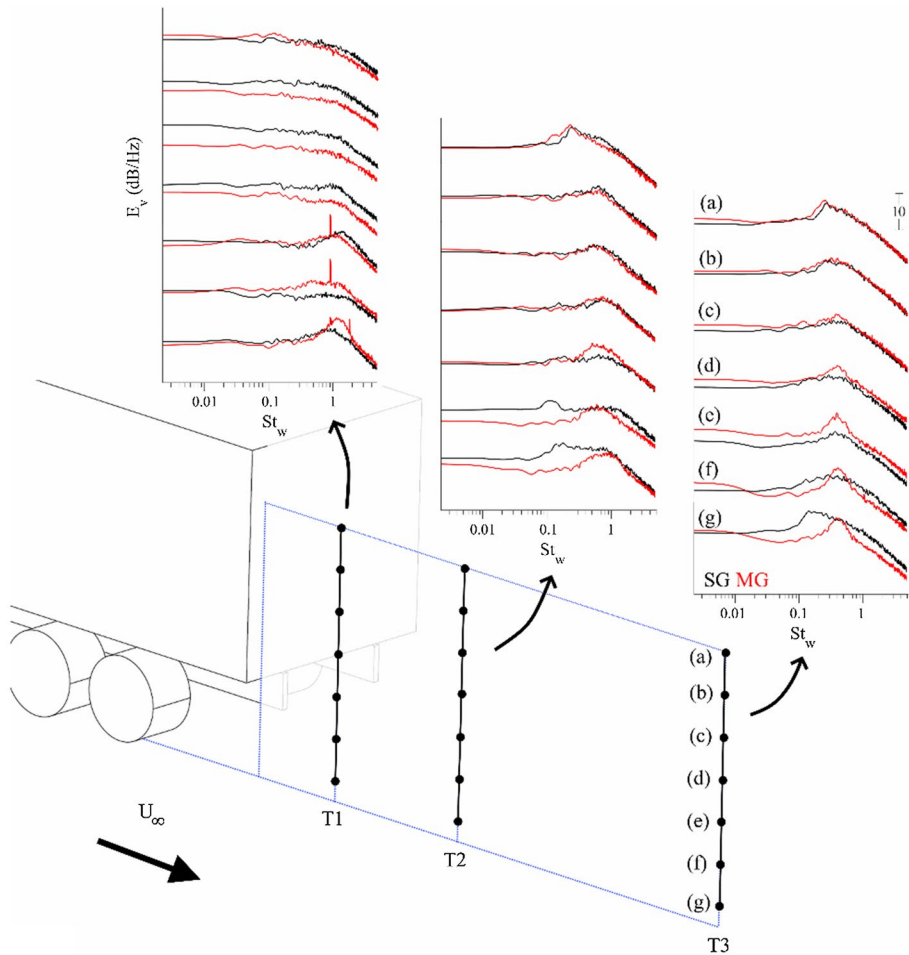
Fig. 19 Streamwise evolution of wheel influence on E_v at $y^* = -0.41$ between $0.091 < z^* < 1.18$

defined spectral behaviour with similar characteristics found at position (g) with use of a stationary ground. This suggests an uplifted wheel wake under these conditions; the flow being entrained through the upwash generated by the GSR. This agrees with the topology presented in Fig. 10. E_ω also shows similar peak magnitudes representing the wheel wake (c–f) as well as the GSR influence (d–e).

The streamwise evolution of E_v is finally considered in Fig. 19. The lowest three positions at T1 (e–g) all show the dominating influence of wheel turbulence ($1 < St_w < 1.2$). This influence is shown to extend heightwise from the ground level to both bottom base corners, confirming results observed in Fig. 6. No direct wheel wake influence at higher locations is obvious although spectral magnitudes are nominally higher in magnitude within the base wake with stationary ground use confirming previously identified trends of increased flow unsteadiness. At location (a), there is little sign of any appreciable effect.

Further downstream to T2, the wheel wake signature is again most distinct at positions (e–g), being decidedly more narrowband, and with a reduced frequency band

$(0.6 < St_w < 0.8)$ with moving ground use. Similar evidence does not exist with stationary ground test conditions, instead, E_v exhibits broader frequency characteristics more representative of turbulence fluctuations within a boundary layer. This suggests the possibility such interactions hasten streamwise dissipation.

The furthest downstream plane (T3) shows the continuing devolution of wheel wake spectra to lower frequencies ($St_w \approx 0.4$). Heightwise propagation increases markedly up to position (c) with moving ground use, with progressively broader spectra at height. E_v also shows the wheel wake influence extends to above half model height at (c) for these test conditions. Conversely results for the stationary ground case show much broader, lower magnitudes confined nearer the ground (particularly e–g) continuing the trend found at T2. In both cases, while streamwise development is decidedly different, there is a clear transition with height from the dominating influence of the wheel wake (g) near the ground to weak crosswise shedding near the top at (a) identified in Figs. 15, 16.

4 Conclusions

An experimental study was conducted on a 1/24th-scale commercial vehicle model to investigate the influence of differing ground simulation conditions on unsteady wake development. Tests were conducted at a Reynolds number, based on vehicle width, of $Re_W = 2.3 \times 10^5$ at high solid model blockage ratio (11.1%). Fully rotating wheels in contact with the ground were included. Drag, base surface pressures, and wake velocities were all measured and compared, with a detailed spectral analysis used to identify and characterise differences in the unsteady flow physics.

Measurements made of total model and trailer drag respectively both showed small reductions with moving ground use; the former being within experimental uncertainty. Base pressure distributions also indicated a reduced wake influence, and reduced unsteadiness under the same conditions. Spatial base pressure gradient distributions further captured the influence of wheel wakes being most significant at both bottom edge trailer base corners with subtle crosswise and heightwise sensitivities identified.

A dominating region of flow separation is shown to develop directly behind the model under stationary ground conditions in-line with previous investigations. This feature was found to promote the generation of significant upwash, producing enhanced crosswise flow localised within the wheel/trailer interface. This effect causes a localised lateral wake contraction which disrupts wheel wake formation. This distortion persists downstream modifying the general wake form to have more inconsistent width with height. Conversely, with moving ground use, the ground separation region is inhibited, promoting unhindered trailer base and wheel wake development.

The time-dependent wake characteristics were found largely absent of strongly defined oscillatory behaviour. Instead, broader flow characteristics were typical. The bubble pumping mode dominated the underlying wake physics and showed a dependency to ground condition. This change showed excellent agreement to the change observed in wake length. For the stationary ground test case, weak asymmetric shedding (flapping) from both horizontal and vertical base edges were identified at $St_w \approx 0.356$ and $St_w \approx 0.279$ respectively; both reducing to $St_w \approx 0.228$ with use of a moving ground. For the latter, stronger, more defined oscillatory flow characteristics, were typical, with the shedding process from vertical base edges revealed to be height-dependent.

Detailed spectral analysis of the region of ground separation revealed source characteristics dominated by low frequencies ($St_w < 0.5$) with spectral magnitudes up to 10 dB higher than that observed when absent. These qualities were found largely irrespective of direction, unveiling this feature as an almost omni-directional source of unsteadiness that contaminates the surrounding flow field.

Wheel wake development was also shown sensitive to ground condition, with use of a moving ground indicating stronger, and more defined shedding than that observed with use of a stationary ground. For the former, signatures were found above model mid-height, more than two-and-a-half model widths downstream. Conversely, for the latter, wheel wakes develop with a lower heightwise influence, being less defined, and dissipated more quickly with downstream propagation.

Overall, these results show that while the time-independent nature of many important performance variables to different ground simulation techniques is often very subtle, and therefore open to a negligible interpretation for simplicity, for utmost validity and fidelity, a full and comprehensive understanding of the flow physics, including detailed spectral insights, should be obtained.

Compliance with ethical standards

Conflict of Interest The authors declare that they have no conflict of interest.

References

Anbarci, K., Acikgoz, B., Aslan, R., Arslan, O., et al.: Development of an aerodynamic analysis methodology for tractor-trailer class heavy commercial vehicles. SAE Int. J. Commer. Veh. (2013). https://doi.org/10.4271/2013-01-2413

Bayraktar, I., Bayraktar, T.: Guidelines for CFD simulations of ground vehicle aerodynamics. SAE Technical Paper 2006-01-3544 (2006). https://doi.org/10.4271/2006-01-3544

Bayraktar, I., Landman, D., Cary, W.K., Wood, R. et al.: An assessment of drag reduction devices for heavy trucks using design of experiments and Computational Fluid Dynamics. SAE Technical Paper 2005-01-3526 (2005). https://doi.org/10.4271/2005-01-3526

Britcher, C., Mokhtar, W., Way, S.: Simulation considerations for commercial vehicles in strong crosswind conditions. SAE Technical Paper 2014-01-2452 (2014). https://doi.org/10.4271/2014-01-2452

Burgin, K., Adey, P.C., Beatham, J.P.: Wind tunnel tests on road vehicle models using a moving belt simulation of ground effect. J. Wind Eng. Ind. Aerodyn. **22**(2–3), 227–236 (1986). https://doi.org/10.1016/0167

Castelain, T., Michard, M., Szmigiel, M., Chacaton, D., Juvé, D.: Identification of flow classes in the wake of a simplified truck model depending on the underbody velocity. J. Wind Eng. Ind. Aerodyn. **175**, 352–363 (2018). https://doi.org/10.1016/j.jweia.2018.02.004

Chandrsuda, C., Bradshaw, P.: Turbulence structure of a reattaching mixing layer. J. Fluid Mech. **110**, 171–194 (1981). https://doi.org/10.1017/S0022112081000670

Cogotti, A.: Ground effect of a simplified car model in side-wind and turbulent flow. SAE Technical Paper 1999-01-0652 (1999). https://doi.org/10.4271/1999-01-0652

Cooper, K.R.: Commercial vehicle aerodynamic drag reduction: Historical perspective as a guide. In: McCallen, R., et al. (eds.) The Aerodynamics of Heavy Vehicles: Trucks, Buses, and Trains. Springer, Berlin, Heidelberg (2004)

Department for Transport: Vehicle Licensing Statistics: Annual 2017 (Revised). UK Government. https://www.gov.uk/government/ statistics/vehicle-licensing-statistics-2017 (2018). Accessed 20 Oct 2019

Devesa, A., Indinger, T.: Fuel consumption reduction by geometry variations on a generic tractor-trailer configuration. SAE Int. J. Commer. Veh. (2012). https://doi.org/10.4271/2012-01-0105

Duell, E.G., George, A.R.: Measurements in the unsteady near wakes of ground vehicle bodies. SAE Technical Paper 930298 (1993). https://doi.org/10.4271/930298

Duell, E.G., George, A.R.: Experimental study of a ground vehicle body unsteady near wake. SAE Technical Paper 1999-01-0812 (1999). https://doi.org/10.4271/1999-01-0812

Fago, B., Lindner, H., Mahrenholtz, O.: The effect of ground simulation on the flow around vehicles in wind tunnel testing. J. Wind Eng. Ind. Aerodyn. **38**, 47–57 (1991). https://doi.org/10.1016/0167-6105(91)90026-S

Forbes, D., Page, G., Passmore, M., Gaylard, A.: A study of computational methods for wake structure and base pressure prediction of a generic SUV model with fixed and rotating wheels. Proc IMechE Part D: J Automob. Eng. **231**(9), 1222–1238 (2017). https://doi.org/10.1177/0954407016685496

Frank, T., Turney, J.: Aerodynamics of commercial vehicles. In: Dillmann, A., Orellano, A. (eds.) The Aerodynamics of Heavy Vehicles III: Trucks, Buses and Trains (2016). https://doi.org/10.1007/978-3-319-20122-1

Geropp, D., Odenthal, H.: Drag reduction of motor vehicles by active flow control using the Coanda effect. Exp. Fluids **28**, 74–85 (2000). https://doi.org/10.1007/s003480050010

Grandemange, M., Gohlke, M., Cadot, O.: Turbulent wake past a three-dimensional blunt body. Part 1. Global modes and bi-stability. J. Fluid Mech. **722**, 51–84 (2013). https://doi.org/10.1017/jfm.2013.83

Grover, K., Visser, K.D.: Over-the-road tests of sealed aft cavities on tractor trailers. SAE Technical Paper 2006-01-3529 (2006). https://doi.org/10.4271/2006-01-3529

Gutierrez, W., Hassan, B., Croll, R., Rutledge, W.: Aerodynamics overview of the Ground Transportation Systems (GTS) project for heavy vehicle drag reduction. SAE Technical Paper 960906 (1996). https://doi.org/10.4271/960906

HM Government: The Carbon Plan: Delivering our Low Carbon Future. Department of Energy & Climate Change, UK Government. https://www.ukgbc.org (2011). Accessed 20 Oct 2019

Horrigan, K., Duncan, B., Sivakumar, P., Gupta, A. et al.: Aerodynamic simulations of a class 8 heavy truck: Comparison to wind tunnel results and investigation of blockage influences. SAE Technical Paper 2007-01-4295 (2007). https://doi.org/10.4271/2007-01-4295

Horrigan, K., Duncan, B., Keating, A., Gupta, A. et al.: Aerodynamic simulations of a generic tractor-trailer: Validation and analysis of unsteady aerodynamics. SAE Technical Paper 2008-01-2612 (2008). https://doi.org/10.4271/2008-01-2612

Hucho, W., Sovran, G.: Aerodynamics of road vehicles. Annu. Rev. Fluid Mech. **25**, 485–537 (1993)

Jørgensen, F.E.: How to measure turbulence with hot-wire anemometers—a practical guide. Dantec Dyn. 19–20 (2002)

Khalighi, B., Zhang, S., Koromilas, C., et al.: Experimental and computational study of unsteady wake flow behind a bluff body with a drag reduction device. SAE Technical Paper 2001-01-1042 (2001). https://doi.org/10.4271/2001-01-1042

Krajnović, S., Davidson, L.: Influence of floor motions in wind tunnels on the aerodynamics of road vehicles. J. Wind Eng. Ind. Aerodyn. **93**(9), 677–696 (2005). https://doi.org/10.1016/j.jweia.2005.05.002

Krajnović, S., Davidson, L.: Large-Eddy Simulation of the flow around simplified car model. SAE Technical Paper 2004-01-0227 (2004). https://doi.org/10.4271/2004-01-0227

Lajos, T., Preszler, L., Finta, L.: Effect of moving ground simulation on the flow past bus models. J. Wind Eng. Ind. Aerodyn. **22**, 271–277 (1986). https://doi.org/10.1016/0167-6105(86)90090-5

Le Good, G.M., Passmore, M.A., Cogotti, A.: A Comparison of on-road aerodynamic drag measurements with wind tunnel data from pininfarina and MIRA. SAE Technical Paper 980394 (1998). https://doi.org/10.4271/980394

Leuschen, J.: The effects of ground simulation on tractor-trailer combinations. SAE Int. J. Commer. Veh. (2013). https://doi.org/10.4271/2013-01-2454

Leuschen, J., Cooper, K.R.: Full scale wind tunnel tests of production and prototype, second-generation aerodynamic drag-reducing devices for tractor-trailers. SAE Technical Paper 2006-01-3456 (2006). https://doi.org/10.4271/2006-01-3456

Lumley, J.L.: The structure of inhomogeneous turbulent flow. In: Yaglom, A.M., Tatarski, V.I. (eds.) Atmospheric Turbulence and Radio Wave Propagation, pp. 166–178. Nauka, Moscow (1967)

Martini, H., Gullberg, P., Lofdahl, L.: Comparative studies between CFD and wind tunnel measurements of cooling performance and external aerodynamics for a heavy truck. SAE Int. J. Commer. Veh. (2014). https://doi.org/10.4271/2014-01-2443

McArthur, D., Burton, D., Thompson, M., Sheridan, J.: On the near wake of a simplified heavy vehicle. J. Fluids Struct. **66**, 293–314 (2016). https://doi.org/10.1016/j.jfluidstructs.2016.07.011

McCallen, R., Couch, R., Hsu, J., Browand, F. et al.: Progress in reducing aerodynamic drag for higher efficiency of heavy duty trucks (Class 7-8). SAE Technical Paper 1999-01-2238 (1999). https://doi.org/10.4271/1999-01-2238

McCallen, R., Flowers, D., Dunn, T., Owens, J. et al.: Aerodynamic drag of heavy vehicles (Class 7–8): Simulation and benchmarking. SAE Technical Paper 2000-01-2209 (2000). https://doi.org/10.4271/2000-01-2209

Mercker, E.: A blockage correction for automotive testing in a wind tunnel with closed test section. J. Wind Eng. Ind. Aerodyn. **22**(2–3), 149–167 (1986). https://doi.org/10.1016/0167-6105(86)90080-2

Mercker, E., Wiedemann, J.: Comparison of different ground simulation techniques for use in automotive wind tunnels. SAE Trans. **99**, 495–509 (1990)

National Statistics: Final UK greenhouse gas emissions national statistics: 1990–2017. Department for Business, Energy & Industrial Strategy. https://www.gov.uk/government/collections/final-uk-greenhouse-gas-emissions-national-statistics (2019). Accessed 20 Oct 2019

Pankajakshan, R., Hilbert, C.B., Whitfield, D.: Passive devices for reducing base pressure drag in Class 8 trucks. In: Dillmann, A., Orellano, A. (eds.) The Aerodynamics of Heavy Vehicles III: Trucks, Buses and Trains (2016). https://doi.org/10.1007/978-3-319-20122-1

Patten, J., Mcauliffe, B., Mayda, W., Tanguay, B.: Review of aerodynamic drag reduction devices for heavy trucks and buses. Technical Report CSTT-HVC-TR-205 (2012)

Pavia, G., Passmore, M.A., Sardu, C.: Evolution of the bi-stable wake of a square-back automotive shape. Exp. Fluids **59**, 1–20 (2017)

Pavia, G., Passmore, M.: Characterisation of Wake Bi-stability for a Square-Back Geometry with Rotating Wheels. FKFS-Conference, Progress in Vehicle Aerodynamics and Thermal Management, pp. 93–109. (2018). https://doi.org/10.1007/978-3-319-67822-1_6

Perry, A.K., Pavia, G., Passmore, M.: Influence of short rear end tapers on the wake of a simplified square-back vehicle: wake topology and rear drag. Exp. Fluids **57**(11), 1–17 (2016). https://doi.org/10.1007/s00348-016-2260-3

SAE International: SAE wind tunnel test procedure for trucks and buses (J1252). SAE Int. (2012). https://doi.org/10.4271/J1252_201207

Salati, L., Cheli, F., Schito, P.: Heavy truck drag reduction obtained from devices installed on the trailer. SAE Int. J. Commer. Veh. (2015). https://doi.org/10.4271/2015-01-2898

Sardou, M.: "Reynolds Effect" and "Moving Ground Effect" tested in a quarter scale wind tunnel over a high speed moving belt. J. Wind Eng. Ind. Aerodyn. **22**, 245–270 (1986). https://doi.org/10.1016/0167-6105(86)90089-9

Sardou, M.: Moving ground and reynolds effect on tractor-trailer. SAE Technical Paper 870707 (1987)

Sims-Williams D.B., Dominy R.: Experimental investigation into unsteadiness and instability in passenger car aerodynamics. SAE Technical Paper 980391 (1998). https://doi.org/10.4271/980391

Söderblom, D., Lofdahl, L., Elofsson, P., Hjelm, L.: An investigation of the aerodynamic drag mechanisms due to ground simulation in yawed flow conditions for heavy trucks. ASME 2009 Fluids Engineering Division Summer Meeting, pp. 1–7. (2009)

Söderblom, D., Elofsson, P., Hjelm, L., Lofdahl, L.: Experimental and numerical investigation of wheel housing aerodynamics on heavy trucks. SAE Int. J. Commer. Veh. **5**(1), 29–41 (2012). https://doi.org/10.4271/2012-01-0106

Söderblom, D., Elofsson, P., Hyvärinen, A.: Numerical investigation of blockage effects on heavy trucks in full scale test conditions. SAE Technical Paper 2016-01-1607 (2016). https://doi.org/10.4271/2016-01-1607

Stephens, R.G., Babinsky, H.: An Experimental study on truck side-skirt flow. SAE Int. J. Passeng. Cars Mech. Syst. **9**(2), 625–637 (2016). https://doi.org/10.4271/2016-01-1593

Storms, B.L., Ross, J.C., Heineck, J.T. et al.: An experimental study of the Ground Transportation System (GTS) model in the NASA Ames 7- by 10-foot wind tunnel. NASA Technical Memorandum 2001–209621 (2001)

Strachan, R.K., Knowles, K., Lawson, N.J.: The vortex structure behind an Ahmed reference model in the presence of a moving ground plane. Exp. Fluids **42**(5), 659–669 (2007). https://doi.org/10.1007/s00348-007-0270-x

Volpe, R., Devinant, P., Kourta, A.: Experimental characterization of the unsteady natural wake of the full-scale square back Ahmed body: flow bi-stability and spectral analysis. Exp. Fluids **56**(5), 1–22 (2015). https://doi.org/10.1007/s00348-015-1972-0

Waeschle, A.: The influence of rotating wheels on vehicle aerodynamics - numerical and experimental investigations. 2007-01-0107 (2007). https://doi.org/10.4271/2007-01-0107

Wang, Y., Sicot, C., Borée, J., Grandemange, M.: Experimental study of wheel-vehicle aerodynamic interactions. J. Wind Eng. Ind. Aerodyn. **198**, 1–15 (2020). https://doi.org/10.1016/j.jweia.2019.104062

Wickern, G., Zwicker, K., Pfadenhauer, M.: Rotating wheels—their impact on wind tunnel test techniques and on vehicle drag results. SAE Trans. **106**, 254–270 (1997)

Wiedemann, J., Potthoff, J.: The new 5-belt road simulation system of the IVK wind tunnels - design and first results. SAE Trans. **112**, 356–374 (2003)

Wiedemann, J.: The influence of ground simulation and wheel rotation on aerodynamic drag optimization—potential for reducing fuel consumption. SAE Technical Paper 960672 (1996). https://doi.org/10.4271/960672

Willemsen, E., Pengel, K., Holthusen, H., Küpper, A.: Automotive testing in the German-Dutch wind tunnels. In: Chiaberge, P. (ed.) New Trends and Recent Developments in Automotive Engineering (2011). https://doi.org/10.5772/13177

Wood, R.: Reynolds number impact on commercial vehicle aerodynamics and performance. SAE Int. J. Commer. Veh. **8**(2), 590–667 (2015). https://doi.org/10.4271/2015-01-2859

Zdravkovich, M.M.: Flow around circular cylinders: Volume II: Applications". Oxford Science Publications, OUP Oxford (2003). ISBN 10: 0198565615

Zdravkovich, M.M.: Flow around circular cylinders: Volume I: Fundamentals. Oxford Science Publications, OUP Oxford (1997). ISBN 10: 0198563965

Zhang, Y.C., Ren, L.L., Pan, K.C., Zhang, Z.: Aerodynamic characteristics of sedan with the rolling road ground effect simulation system. Veh. Eng. **2**, 31–35 (2014)